

Thermoelectric sintered glass-ceramics with a $\text{Bi}_2\text{Sr}_2\text{Co}_2\text{O}_x$ phase

Julian Lingner^{1,3} · Ryoji Funahashi² · Emmanuel Combe² · Martin Letz³ · Gerhard Jakob¹

Received: 5 December 2014 / Accepted: 8 April 2015 / Published online: 24 April 2015
© Springer-Verlag Berlin Heidelberg 2015

Abstract Glass-ceramic materials containing $\text{Bi}_2\text{Sr}_2\text{Co}_2\text{O}_x$ crystals with plate-like structures are prepared by a melting process and a subsequent sintering step after manual quenching. The chemical starting compositions of the samples are $\text{Bi}_2\text{Sr}_2\text{Co}_2\text{O}_x$ (BSC222), $\text{Bi}_{1.8}\text{Sr}_2\text{Co}_2\text{O}_x$ (Bi1.8) and $\text{Bi}_2\text{Sr}_2\text{Co}_{1.7}\text{O}_x$ (Co1.7). All three samples are p-type conductors. The electric properties of Seebeck coefficient S and electrical resistivity ρ show only a slight dependence on chemical composition. The Seebeck values increase with increasing temperature, and at $T = 873$ K, they reach $S = 180$, 176 and 167 $\mu\text{V}/\text{K}$, respectively. The electrical resistivity slightly decreases with temperature for two samples and increases for the Co1.7 sample. The thermal conductivity for all measured samples at this temperature is around $\kappa = 0.8$ $\text{W}/(\text{m K})$. The figure of merit ZT increases with temperature for all samples. The materials reach a ZT value of 0.03 at $T = 873$ K.

1 Introduction

The global search for a way of more sustainable usage of natural resources is becoming the focus of attention due to the predicted growing energy demand. By 2040, the world

energy consumption will have grown by over 56 % compared to 2010. A large increase in this energy use will come from non-OECD nations, and it is predicted that despite the projected high world oil prices, fossil fuels will still be the major supplier of the overall energy [1]. Thermoelectric generators are considered to be one of the promising candidates to make use of the enormous amounts of waste heat, which occur, for example, in industrial processes, by converting this excess heat into electric power [2]. State-of-the-art materials that are used in such generators are Bi_2Te_3 , PbTe or SiGe [3]. Despite being well established, those materials have different drawbacks like low operating temperatures and environmentally harmful or expensive components. These are reasons that large-scale thermoelectric generators are not used in a broad application range as of today [4].

When the cobalt oxide compounds were discovered as possible high-temperature thermoelectric materials around 15 years ago, the material class of oxides was quickly considered to be a promising “clean” alternative to existing and established solutions. The reason for the good performance of the layered cobalt oxides like $\text{Na}_x\text{Co}_2\text{O}_4$ [5] and $\text{Ca}_3\text{Co}_4\text{O}_9$ [6], which showed metallic electrical resistivity ρ while maintaining a high Seebeck coefficient S , is the quasi-two-dimensionality of the layered structure and therefore the enhancement of the electronic density of states, which is beneficial to the charge carrier density. Also because the different spin states in Co^{3+} and Co^{4+} lead to large carrier entropy, the Seebeck coefficient S benefits from these systems [7]. In addition, the large unit cell of compounds like $\text{Ca}_3\text{Co}_4\text{O}_9$ results in many optical phonon modes with low dispersion; therefore, the material offers a low thermal conductivity κ .

Since the thermoelectric performance is usually evaluated by the figure of merit

✉ Julian Lingner
julian.lingner@web.de

¹ Institut für Physik, Johannes Gutenberg-Universität Mainz, 55128 Mainz, Germany

² National Institute of Advanced Industrial Science and Technology, Ikeda, Osaka 563-8577, Japan

³ Material Development, SCHOTT AG, 55122 Mainz, Germany

$$ZT = \frac{S^2}{\rho\kappa} T \quad (1)$$

with T being the absolute temperature, it is obvious from Eq. (1) that it is beneficial to increase the numerator while decreasing the denominator.

$\text{Bi}_2\text{Sr}_2\text{Co}_2\text{O}_x$, which is another promising thermoelectric oxide, consists of layers of SrO and BiO, which are “sandwiched” along the c -axis between CoO_2 blocks [8]. The compound has been synthesized via a partial melting technique [9], a hot pressing process [10] and as nano-whiskers [8] and showed maximum ZT values of 0.19, 0.26 and 1.1, respectively. These values suggest the high potential of this material to be a strong candidate as a p-type oxide thermoelectric material. Bulk materials show lower ZT values than single-crystalline samples. This is due to the high values of ρ . For applications of power generation, bulk devices based on polycrystalline materials are indispensable, and in order to decrease κ , introducing phonon scattering sites is a promising strategy in those materials.

Synthesizing thermoelectric materials from an amorphous precursor is a rather new field, but it promises interesting features like low thermal conductivity due to the residual glassy phase as well as new microstructuring possibilities. Additionally, glass annealing offers the possibility to obtain highly densified bulk materials, where the high density is effective to suppress the electrical resistivity. The exact growth mechanism of the $\text{Bi}_2\text{Sr}_2\text{Co}_2\text{O}_x$ phase, especially from a melt, has not been investigated yet. In order to complete the picture of the already established synthesis routes, this work shows the preparation and characterization of a sintered glass-ceramic material, starting from a complete melt. For this, a partly amorphous precursor material undergoes an annealing process during which the desired $\text{Bi}_2\text{Sr}_2\text{Co}_2\text{O}_x$ phase is formed and verified.

2 Experimental steps

To obtain the glassy precursor, powders of SrCO_3 , Bi_2O_3 and Co_3O_4 were mixed in batches of 50 g with the stoichiometry of $\text{Bi}_2\text{Sr}_2\text{Co}_2\text{O}_x$ (BSC222), $\text{Bi}_{1.8}\text{Sr}_2\text{Co}_2\text{O}_x$ (Bi1.8) and $\text{Bi}_2\text{Sr}_2\text{Co}_{1.7}\text{O}_x$ (Co1.7). They were milled in an automatic agate mill twice for 20 min at 300 rpm. The three stoichiometries were chosen in this way to compensate for potential inhomogeneities emerging during or after the subsequent melting process. The powder batch was then put in an aluminum oxide crucible and heated in a high-temperature furnace to 1473 K. After a dwell time of 30 min, the liquefied mixture was taken out of the furnace, casted onto a copper plate and immediately quenched from the top with a second copper plate. In this way, a partly

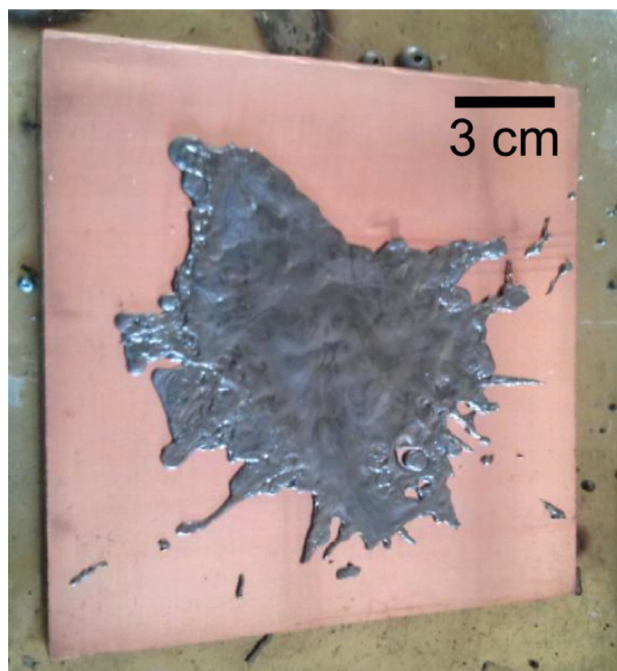


Fig. 1 Picture of a quenched sample

amorphous precursor material was obtained (see Fig. 1), which was checked by energy-dispersive X-ray microanalysis (EDX) for its cationic distribution.

Subsequently, the quenched glassy samples were crushed and then pulverized in an automatic agate mortar. After that, the powders were checked for initial crystal phases by X-ray diffraction (XRD) measurements. The rest of the powders was pressed into pellets of 3 g each ($\varnothing = 16$ mm) using a uniaxial press with a force of 20 kN. Then, the pressed pellets were put on a gold sheet, which was lying on an aluminum shuttle. They were annealed in a muffle furnace under ambient pressure and atmosphere at 1133 K for 15 h. A separate calcination step was not considered since all organic remains were assumed to have vanished during the melting process. After cooling down, the annealed samples were examined via XRD (powder) and scanning electron microscopy (SEM, bulk samples).

For the measurement of the properties, the samples were cut into equally sized rectangular bars using a diamond saw and the resistivity ρ was determined using a DC four-probe method in air. Here, thin platinum wires were attached to the sample surfaces using silver paste as contact, and measurements up to 873 K were taken. Because of the lack of applied pressure during the annealing step and therefore during the phase formation in the material, it was not expected that there would be a distinct parallel alignment of the layers but that they would form rather disordered within the sample. Thus, it was also not expected that there would be a significant difference of the electrical and thermal

properties depending on whether the measurement was taken in parallel or perpendicular to the original pressing direction of the pellet. For reasons of simplicity, the electrical measurements were taken parallel toward the pressing plane.

Then, the thermovoltage at a known temperature difference was measured, and by taking the absolute Seebeck values of the thermocouples into account, the Seebeck coefficient S was calculated. For the contacts on the samples, silver pastes in combination with Pt and Pt–Rh thermocouples were used. These measurements were taken in air atmosphere from room temperature up to 873 K. According to [11], the measurement errors of the electrical properties originate from the inaccuracy of the thermocouples, the geometry variations of the samples and the averaging over the several data points, which were taken for each temperature step. This accumulates to a total error of about 5 % for the Seebeck coefficient and the electrical resistivity.

The thermal diffusivity α and the specific heat c_p were measured with a laser flash apparatus on rectangular thin samples. Those were each polished down to a thickness of about 0.8 mm and coated with graphite spray for optimized laser absorption. Using the density ρ , the thermal conductivity could be calculated by

$$\kappa = \alpha \rho c_p \quad (2)$$

Due to the fact that each quantity is prone to errors, the total error of the thermal conductivity is assumed to be 10 %.

In order to correlate the thermoelectric measurement results with the magnetic properties of the material, the temperature-dependent susceptibility X was measured using a SQUID magnetometer. For that, small sample specimens (~200 mg) were put in a plastic capsule and the capsule with the sample inside was measured at a field of 1000 Oe from room temperature down to 2 K. A measurement of an empty capsule was taken in order to check for the diamagnetic influence of the capsule material on the result. The contribution was well below 10 % of the result with a sample inside. Because the measurements were primarily targeted at showing the relative differences in susceptibility between the samples, the small capsule influence was neglected during measurement and treated as a systematic error. However, a temperature-independent parameter X_0 was obtained from the fit of the Curie–Weiss law to the measurement data later on.

3 Results

Just as expected, there was a deviation between the starting compositions and measured cation ratio after the casting. This was due to the fact that the melt was in contact with

the crucible material. Therefore, an unknown amount of Al was dissolved and changed the overall composition. Sediment inside the crucible could also be observed because when taken out of the furnace, the melt at the bottom solidified too quickly to cast the complete content onto the copper plate. By this, the homogeneity of the precursor material was changed during the melting process as well.

In the interest of simplification, the amount of Al content (2–3 mol%) coming from the dissolving alumina crucible was neglected during the EDX scan. It has to be kept in mind though that a certain amount of Al is inside each sample. We assume that this has helped to form the amorphous structure of the material.

It can be seen from Table 1 that the amount of Co in the casted glassy samples is much higher than in the earlier powder synthesis of said specimen. This is due to the fact that cobalt oxide exists as a solid phase alongside a liquid phase of Bi–Sr–O [12]. Upon casting, most of the cobalt oxide come out, while some of the liquid phase containing Bi–Sr–O remains on the surface of the crucible. Therefore, the Co content of all samples is increased compared with the starting composition.

After quenching the material, the samples were crushed, pelletized and sintered, and XRD measurements were taken to see the difference in phase formation before and after the sintering process. Because all X-ray measurements were taken on powdered sample material, there was no specific preferred direction observed in the diffraction image as it could be found in [9]. When comparing the diffraction data of the sample before and after the sintering step, the formation of the Bi₂Sr₂Co₂O_x phase can be clearly observed (see Fig. 2). Minor unknown crystal phases in the semicrystalline material vanish during sintering in favor of the desired phase of the sinter glass-ceramic material. This is indicated by the Miller indices of Bi₂Sr₂Co₂O_x in Fig. 2, with peak positions taken from Ref. [13].

The layered structure of the material, which is discussed and shown in Ref. [9], is less pronounced in the sintered glass-ceramic material as expected due to the lack of pressure during phase formation.

This is noticeable in the SEM image in Fig. 3, even though not as aligned and evenly distributed. The grain sizes differ between 2 and 10 μm. Among the three

Table 1 EDX results

	Cationic content: starting composition/after quenching		
	Bi	Sr	Co
Sample1 BSC222	2/1.8	2/1.7	2/2.5
Sample2 Bi1.8	1.8/1.7	2/1.9	2/2.4
Sample3 Co1.7	2/2.1	2/1.8	1.7/2.1

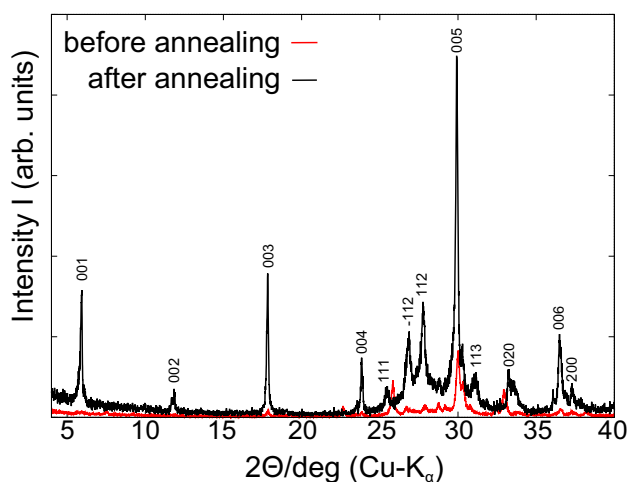


Fig. 2 XRD patterns of BSC222 sample, *red curve* after quenching and before sintering, *black curve* after sintering

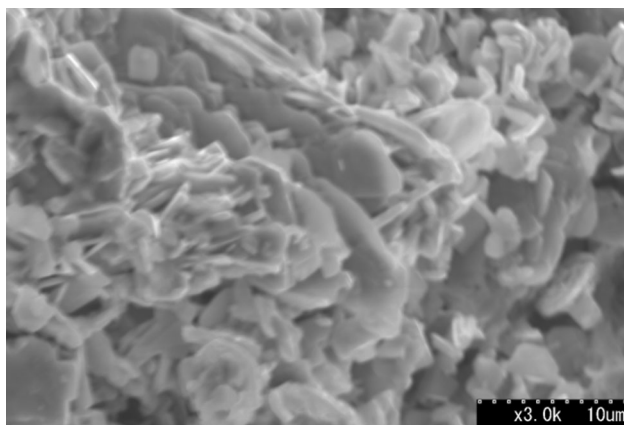


Fig. 3 SEM micrograph of BSC222 bulk material

samples, no distinct difference in microstructure could be observed.

The density of the samples was measured using the Archimedes method to be around $\rho_d = 6.3 \text{ g/cm}^3$ ($\sim 92 \%$ theoretical density). This value is higher than the one from sintered samples prepared by solid-state reactions of BSC222 powders ($<90 \%$, [14]) and emphasizes the advantage of glass annealing. Concerning the measurement results of the electrical resistivity, it is observable that there are some differences between the three samples. The temperature characteristic of sample BSC222 and Co1.7 is rather flat. However, both samples show a small decrease in resistivity until 600 K; above that temperature, the resistivity increases again. A similar behavior was found in [9], where the increase in resistivity started at 750 K though. Sample Bi1.8 shows a rather metallic conductivity with the resistivity increasing with increasing temperature across the whole range. This can be understood as a

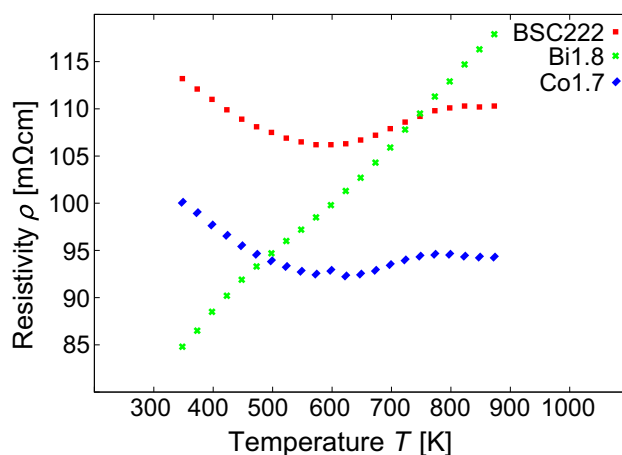


Fig. 4 Temperature dependence of electrical resistivity for the different bulk materials

classical metallic conduction mechanism where the resistivity increases linearly with T . An interesting observation is the fact that the Bi1.8 sample shows the overall lowest resistivity ρ of all the samples at room temperature but changes to have the highest resistivity at maximum temperature (Fig. 4).

In [8], the different slopes of the resistivity measurements were attributed to the different valence states of Co in the samples. Since in this case the cationic composition before and after the melting process differs so much and also the exact oxygen deficiency is unknown, it is impossible to calculate the Co valence to explain the results. If, however, the resistivity and the conduction mechanism are defined by the valence state and the carrier concentration, one might assume that the BSC222 and Co1.7 samples show a similar valence in contrast to Bi1.8. Additionally, the hole concentration in Co1.7 should be higher than in BSC222 because of its lower resistivity. We can observe that the Bi/Sr ratio is >1 at those samples, while it is <1 in the Bi1.8 sample. We see no clear possibility though how this can explain the metallic conductivity. It might be connected with the oxygen content in the final melt.

In Fig. 5, the Seebeck coefficient of the three samples is shown. All measured Seebeck coefficients are positive, which indicates a hole conduction mechanism as expected. With increasing temperature, the values of all three samples increase, which confirms the resistivity data at least from 600 K because for metals an increase in the Seebeck coefficient with increasing temperature is expected (S - T) [15]. Despite the assumed identical Co valence, the Co1.7 sample has a lower S value at 873 K than the BSC222 sample. As in [9], the difference can be explained by the different carrier concentrations over the spin states of Co.

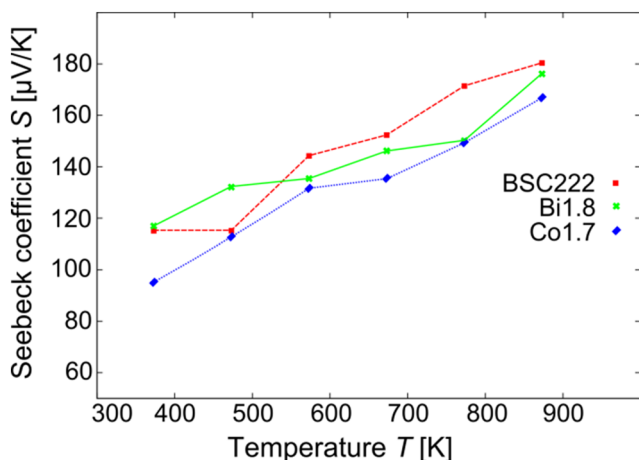


Fig. 5 Temperature dependence of Seebeck coefficient

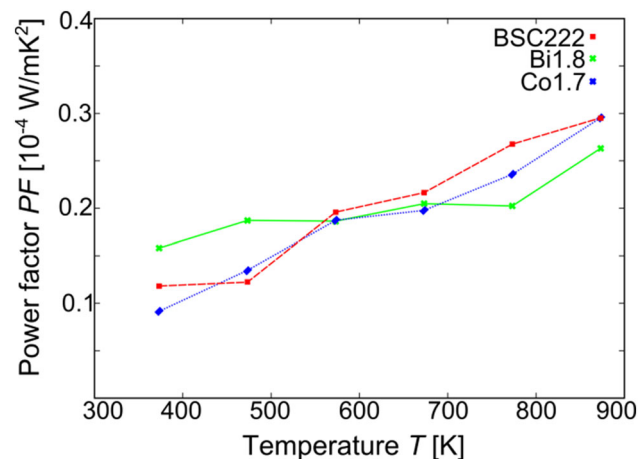


Fig. 6 Temperature dependence of the power factor of the different samples

Figure 6 shows the power factor $PF = S^2/\rho$. For all samples, PF increases with temperature. Because of the increase in resistivity, the power factor of Bi1.8 is below that of BSC222 and Co1.7 at 873 K. A maximum value of $PF = 0.3 \times 10^{-4} \text{ W/m K}^2$ is reached for the BSC222 and Co1.7 samples.

Figure 7 shows the thermal conductivity for the three samples. The temperature dependence is almost linear and increases slightly until 673 K, where a decline of κ can be observed. Again, BSC222 and Co1.7 show a very similar behavior, and their values differ only slightly. As with the electrical conductivity, Bi1.8 shows a different behavior concerning the thermal conductivity. Here, the thermal conductivity increases incrementally with no change in its slope throughout the measured temperature range. Since the electrical resistivity is rather high for all samples, it is assumed that the electronic contribution to the thermal conductivity κ_e is small and that κ consists mostly of the

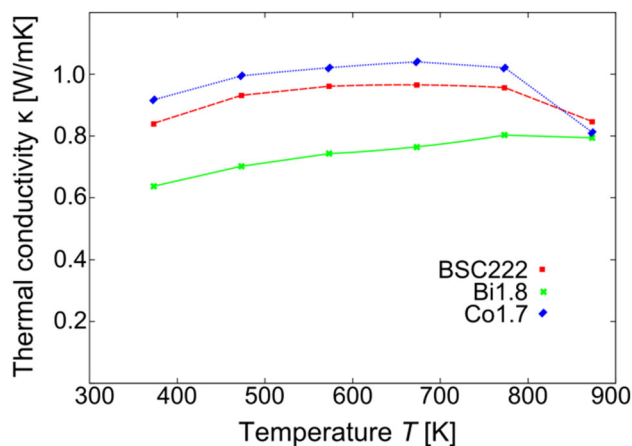


Fig. 7 Temperature dependence of thermal conductivity of the different samples

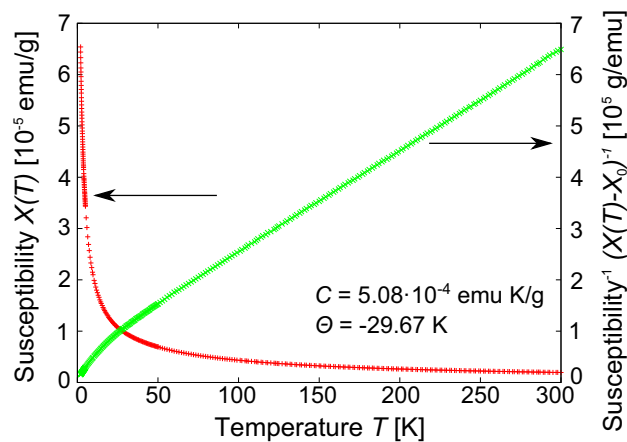


Fig. 8 Susceptibility of Bi1.8 sample

lattice thermal conductivity κ_l . However, the expected decrease in conductivity with increasing temperatures due to enhanced phonon scattering cannot be observed. The value of κ is low despite the high density of the sample, which might be due to residual amorphous parts or minor secondary crystal phases in the samples.

The magnetic measurement of the susceptibility is exemplarily shown for Bi1.8 in Fig. 8. For all samples, the data from $100 \text{ K} < T < 300 \text{ K}$ were fitted using the Curie–Weiss law

$$X = X_0 + \frac{C}{T - \Theta} \tag{3}$$

with X_0 , C and Θ being the temperature-independent susceptibility, the Curie constant and the Curie temperature, respectively. The linear Curie–Weiss behavior can be observed for $T > 100 \text{ K}$. For all samples, the Curie temperature is negative suggesting an antiferromagnetic interaction. Co^{3+} is expected to be in a low spin (LS) state and to have a completely filled t_{2g} band therefore not

contributing to the overall magnetization. Co^{4+} in the LS state has an unfilled band and contributes with $S = 1/2$ plus an electronic degeneracy of $g_{\text{Co}^{4+}} = 6$ [7].

Figure 9 shows the inverse susceptibility of the samples as well as linear fits to the high-temperature data to extrapolate to the Curie temperature. As expected from their compositions, BSC222 and Bi1.8 show a similar susceptibility and Curie temperature. Only Co1.7 that contains a smaller amount of Co compared to the other samples shows a smaller Curie temperature and a higher inverse susceptibility.

In order to estimate the amount of Co^{4+} in the samples, the number of Bohr magnetons per formula unit was compared to a theoretical value that was obtained by using the Brillouin function. For this, the mole number of each sample was calculated from its weight. The number of Bohr magnetons per formula unit was calculated subsequently

$$N_{\text{fu}} = N_{\text{mol}} \times N_A \quad (4)$$

$$N_{\mu\text{Bexp}} = \left(\frac{m}{\mu_B} / N_{\text{fu}} \right) \quad (5)$$

with N_{mol} being the mole number, N_A the Avogadro number, m the magnetic moment and μ_B the Bohr magneton. For the calculation, a value of $x = 9$ has been assumed in $\text{Bi}_2\text{Sr}_2\text{Co}_2\text{O}_x$, since oxygen-rich compounds like Co_3O_4 have been used in the composition and the melt was carried out in air atmosphere.

The theoretical value for the sample containing hypothetically 100 % Co^{4+} with $J = S$ (pure spin magnetism) was calculated using

$$N_{\mu\text{Bth}} = N_{\text{Co}} \times g \times J \times f_B \quad (6)$$

$$f_B = \left(1 + \frac{1}{2J} \right) \coth \left(\left(1 + \frac{1}{2J} \right) x \right) - \left(\frac{1}{2J} \right) \coth \left(\frac{1}{2J} x \right) \quad (7)$$

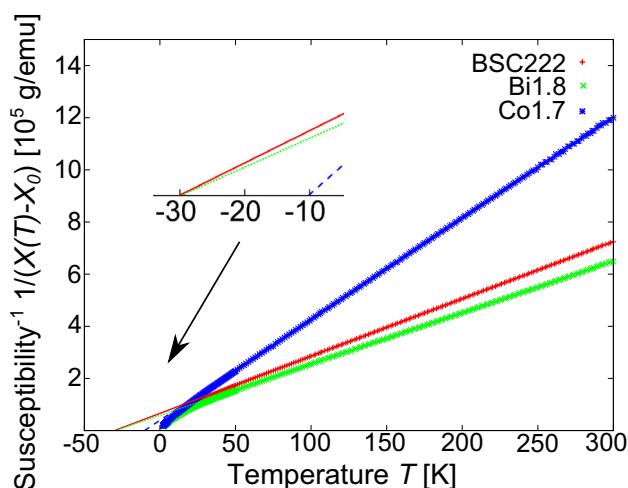


Fig. 9 Susceptibility of all prepared samples

$$x = \frac{g \times \mu_B \times J \times B}{k_B T} \quad (8)$$

where N_{Co} stands for the cationic content of Co per formula unit (obtained from EDX measurements, see Table 1). The Landé factor $g = 2$ and spin $S = 1/2$ are used as well as the Brillouin function f_B , which takes the orientation of the moments into account.

Technically, the Brillouin function is used to describe a paramagnetic substance in an external magnetic field. To account for that, the temperature offset obtained from the Curie–Weiss fits (see Fig. 8) was used.

The obtained value for $N_{\mu\text{Bth}}$ (100 % Co^{4+}) was adjusted with a linear-scale factor y to match the experimental data of $N_{\mu\text{Bexp}}$ in order to find an approximation for the actual amount of Co^{4+} in the investigated sample.

For the three samples, the amount y of Co^{4+} and the average Co valence is shown in Table 2.

From this, it is obvious that only a fraction of the Co ions contributes to the overall signal of the magnetization. For Bi1.8, the metallic behavior in electrical conductivity may be explained by the highest average Co valence and therefore the highest hole concentration. The electrical conductivity of the other samples cannot be explained by this because even though the hole concentration in BSC222 is higher than in Co1.7, its resistivity is higher.

Plotting the Co valence versus ρ , S and the power factor yield the following picture.

Here, the electrical resistivity increases proportionally with the Co valence, while the Seebeck coefficient reaches a maximum value around $\text{Co}^{3.45+}$. Finally, the maximum value of the power factor can be obtained between $\text{Co}^{3.3+}$ and $\text{Co}^{3.45+}$. It can be concluded that among the available samples, lower valences of Co seem to be favorable for obtaining a high power factor. This result agrees with the findings in [9], where a similar conclusion can be drawn when comparing the samples' properties and their average Co valence.

In order to make more use of the obtained valence values, the modified Heikes formula [16] in the high-temperature limit can be applied to calculate the Seebeck coefficient from

$$S = - \frac{k_B}{|e|} \ln \left(\frac{1}{g_{\text{Co}^{4+}}} \frac{y}{1-y} \right) \quad (9)$$

Table 2 Co^{4+} content of the samples

Sample	Co^{4+} fraction	Av. Co valence
BSC222	0.44	3.44
Bi1.8	0.52	3.52
Co1.7	0.30	3.30

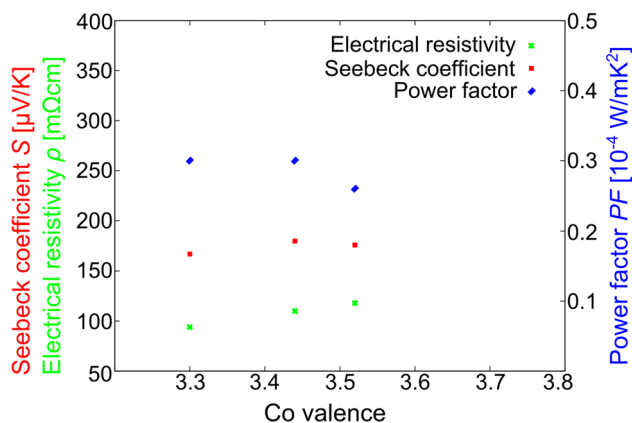


Fig. 10 Correlation of Co valence and thermoelectric properties

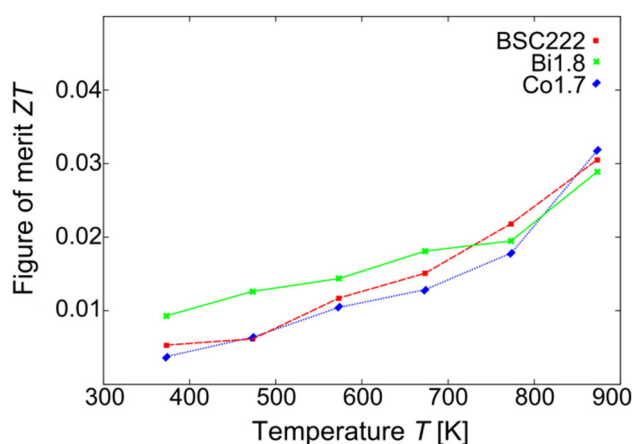


Fig. 11 Change of ZT values with temperature of the different samples

with a degeneracy of $g_{\text{Co}^{4+}} = 6$. The $\text{Co}^{4+}/\text{Co}^{3+}$ ratios found in Table 2 lead to Seebeck values of 148 $\mu\text{V}/\text{K}$ (Bi1.8), 175 $\mu\text{V}/\text{K}$ (BSC222) and 227 $\mu\text{V}/\text{K}$ (Co1.7). Disregarding the latter, the first two seem to match the experimental findings quite well at high temperatures (see Fig. 5).

Because the thermoelectric performance is characterized by the dimensionless figure of merit ZT , the characterization of the material can be done via $ZT = S^2/(\rho \times \kappa) \times T$. The result is shown in Fig. 10. A ZT value of more than 0.03 is reached which is about five times lower than in Ref. [9] (Fig. 11).

4 Conclusions

Sintered glass-ceramic samples with three different cationic compositions have been prepared and measured concerning their thermoelectric and magnetic properties.

While comparing the different samples, a linear correlation between the thermoelectric properties ρ and S and the Co valence could be observed. The worse thermoelectric properties compared with pure ceramic $\text{Bi}_2\text{Sr}_2\text{Co}_2\text{O}_x$ are mainly due to the lack of homogeneity which comes from the production process of simple casting from an alumina crucible as well as the lack of pressure during the annealing treatment.

However, it could be shown that the annealing of a glassy BSC222 powder showed high densities of the sintered body compared to a sintering process of crystalline material. This is favorable for obtaining low resistivities even if those could not be reached due to said sample inhomogeneity. The glass annealing method should be a promising way to decrease ρ and κ if the composition can be optimized. Techniques like melt spinning and the application of pressure during the phase formation process could be helpful in increasing the homogeneity and density/layer structure, which subsequently would improve the thermoelectric properties. In this way, it should also be possible to establish a more precise correlation between the compositional details and their impact on the microstructure. In order to correlate the magnetic properties to the thermoelectric parameters, it would be beneficial to measure the oxygen content in the samples as the uncertainty concerning the number of vacancies complexifies the interpretation of the data.

Acknowledgments The authors would like to thank Dr. Lydia Sosa-Vargas of the National Institute of Advanced Industrial Science and Technology (AIST Ikeda, Osaka) for her help and guidance during the XRD measurements.

References

1. International Energy Outlook 2013, U.S. Energy Information Administration Report Number: DOE/EIA-0484 (2013)
2. S.B. Riffat, X. Ma, Thermoelectrics: a review of present and potential applications. *Appl. Therm. Eng.* **23**(8), 913–935 (2003)
3. G.J. Snyder, E.S. Toberer, Complex thermoelectric materials. *Nat. Mater.* **7**(2), 105–114 (2008)
4. H. Ohta, K. Sugiora, K. Koumoto, Recent progress in oxide thermoelectric materials: p-type $\text{Ca}_3\text{Co}_4\text{O}_9$ and n-type SrTiO_3 . *Inorg. Chem.* **47**(19), 8429–8436 (2008)
5. I. Terasaki, Y. Sasago, K. Uchinokura, Large thermoelectric power in NaCo_2O_4 single crystal. *Phys. Rev. B* **56**(20), 685–687 (1997)
6. R. Funahashi, I. Matsubara, H. Ikuta, T. Takeuchi, U. Mizutani, S. Sodeoka, An oxide single crystal with high thermoelectric performance in air. *Jpn. J. Appl. Phys.* **39**, L1127 (2000)
7. Y. Wang, N.S. Rogado, R.J. Cava, N.P. Ong, Spin entropy as the likely source of enhanced thermopower in $\text{Na}_x\text{Co}_2\text{O}_4$. *Nature* **423**(6938), 425–428 (2003)
8. R. Funahashi, M. Shikano, $\text{Bi}_2\text{Sr}_2\text{Co}_2\text{O}_y$ whiskers with high thermoelectric figure of merit. *Appl. Phys. Lett.* **81**, 1459–1461 (2002)

9. R. Funahashi, I. Matsubara, S. Sodeoka, Thermoelectric properties of $\text{Bi}_2\text{Sr}_2\text{Co}_2\text{O}_x$ polycrystalline materials. *Appl. Phys. Lett.* **76**(17), 2385–2387 (2000)
10. G. Xu, R. Funahashi, M. Shikano, I. Matsubara, Y. Zhou, Thermoelectric properties of $\text{Bi}_{2.2-x}\text{Pb}_x\text{Sr}_2\text{Co}_2\text{O}_y$ system. *J. Appl. Phys.* **91**(7), 4344–4347 (2002)
11. S. Populoh, M.H. Aguirre, O.C. Bruner, K. Galazka, Y. Lu, A. Weidenkaff, High figure of merit in (Ti, Zr, Hf)NiSn half-Heusler alloys. *Scr. Mater.* **66**, 1073–1076 (2012)
12. O. Jankovský, D. Sedmidubský, Z. Sofer, Phase diagram of the pseudobinary system Bi–Co–O. *J. Eur. Ceram. Soc.* **33**(13–14), 2699–2704 (2013)
13. A. Sotelo, M.A. Torres, G. Constantinescu, S. Rasekh, J.C. Diez, M.A. Madrea, Effect of Ag addition on the mechanical and thermoelectric performances of annealed $\text{Bi}_2\text{Sr}_2\text{Co}_{1.8}\text{O}_x$ textured ceramics. *J. Eur. Ceram. Soc.* **32**(14), 3745–3751 (2012)
14. R. Funahashi, Unpublished data (2014)
15. N. Cusack, P. Kendrall, The absolute scale of thermoelectric power at high temperature. *Proc. Phys. Soc. Lond.* **72**(5), 898–901 (1958)
16. Y. Klein, D. Pelloquin, S. Hébert, A. Maignan, J. Hejtmanek, Thermoelectric $[\text{Sr}_2(\text{Bi}, \text{Co})_n - 2\text{O}_n]\text{RS}[\text{CoO}_2]_{1.8}$ layer cobaltates—the role of the intergrowth between the $n = 3$ and $n = 4$ terms. *J. Appl. Phys.* **98**(1), 013701 (2005)